

On the velocity drift between ions in the solar atmosphere

JUAN MARTÍNEZ-SYKORA,^{1,2,3} MIKOLAJ SZYDLARSKI,^{3,4} VIGGO H. HANSTEEN,^{1,2,3,4} AND BART DE PONTIEU^{1,3,4}

¹*Lockheed Martin Solar & Astrophysics Laboratory, 3251 Hanover St, Palo Alto, CA 94304, USA*

²*Bay Area Environmental Research Institute, NASA Research Park, Moffett Field, CA 94035, USA*

³*Roseland Centre for Solar Physics, University of Oslo, P.O. Box 1029 Blindern, NO0315 Oslo, Norway*

⁴*Institute of Theoretical Astrophysics, University of Oslo, P.O. Box 1029 Blindern, N-0315 Oslo, Norway*

Submitted to ApJ

ABSTRACT

The solar atmosphere is composed of many species which are populated at different ionization and excitation levels. The upper chromosphere, transition region and corona are nearly collisionless. Consequently, slippage between, for instance, ions and neutral particles, or interactions between separate species, may play important roles. We have developed a 3D multi-fluid and multi-species numerical code (*Ebysus*) to investigate such effects. *Ebysus* is capable of treating species (*e.g.*, hydrogen, helium etc) and fluids (neutrals, excited and ionized elements) separately, including non-equilibrium ionization, momentum exchange, radiation, thermal conduction, and other complex processes in the solar atmosphere. Treating different species as different fluids leads to drifts between different ions and an electric field that couples these motions. The coupling for two ionized fluids can lead to an anti-phase rotational motion between them. Different ionized species and momentum exchange can dissipate this velocity drift, *i.e.*, convert wave kinetic energy into thermal energy. High frequency Alfvén waves driven by, *e.g.*, reconnection thought to occur in the solar atmosphere, can drive such multi-ion velocity drifts.

Keywords: Magnetohydrodynamics (MHD) — Methods: numerical — Radiative transfer — Sun: atmosphere — Sun: corona

1. INTRODUCTION

To study the outer atmosphere of the Sun and in particular, the interaction between the magnetic field and plasma a single fluid magnetohydrodynamic (MHD) treatment is often chosen. This is usually sufficient, however, single-fluid MHD process timescales may become comparable to collision frequencies or the presence of neutrals may dominate the dissipation processes in the atmosphere. As one progresses upwards in the solar atmosphere, and especially into the relatively cold, tenuous solar chromosphere, a multi-fluid magnetohydrodynamic (MHD) treatment of the plasma and magnetic field becomes increasingly relevant in order to handle many aspects of the weakly ionized, weakly collisional medium. For instance, the high-fraction of neutral particles in the chromosphere may play an important role, and drift velocities between different fluids may be too important to neglect (Vernazza *et al.* 1981;

Fontenla *et al.* 1990; Leake *et al.* 2014; Martínez-Sykora *et al.* 2015, 2017b; Ballester *et al.* 2018). Some studies have already gone beyond a single fluid approach, and these can be categorized into two groups: First, in a weakly ionized plasma with ion-neutral collision timescales small enough, one can assume that ion-neutral interactions effects can be approximated through an expansion of Ohm’s law (see Cowling 1957; Braginskii 1965; Parker 2007, amongst others) by including ambipolar diffusion (Biermann 1950) into the single fluid MHD equations, (*e.g.*, Leake *et al.* 2005; Cheung & Cameron 2012; Khomenko & Collados 2012; Martínez-Sykora *et al.* 2012; Leake & Linton 2013; Martínez-Sykora *et al.* 2017c; Nóbrega-Siverio *et al.* 2020b). The second group of studies treats ions and neutrals as two completely different fluids (*e.g.*, Brandenburg & Zweibel 1994, 1995; Lazarian *et al.* 2004; Leake *et al.* 2013; Alvarez Laguna *et al.* 2016, 2017; Maneva *et al.* 2017) with separate velocities and energies, only coupled through collisions.

The solar atmosphere consists of large variety of species and most previous studies have typically assumed that species can be treated as a single or two

fluids. Chapman & Cowling (1970) derived the single fluid equations from a multi-species description. This required the assumption that all species move in unison, which it is not necessarily the case in a weakly collisional environment. Furthermore physical processes are different depending on the ionization state of the species under consideration (see Sections 2 and 3.1). Khomenko et al. (2014) and Ballester et al. (2018) describe the full set of MHD equations separately for each species. This description is better suited to describing the plasma when collisional interactions between species are weak.

Under the conditions where collisional interactions between species are weak, a physical processes due to electromagnetic interactions between ionized species become important. Alfvén waves exhibit one mode that does not appear in single-ion plasma (a fluid with a single ionized species Weber 1973; Cramer 2001). The frequency of this mode is known as weighted average ion-cyclotron frequency of the different ionized species participating in the wave motion (in this paper, we refer to this as the multi-ion cyclotron frequency). The mode can be dissipated by the momentum exchange between species (Isenberg & Hollweg 1982; Hollweg & Isenberg 2002; Rahbarnia et al. 2010; Martínez-Gómez et al. 2016, 2017). Ionized species are accelerated by a non-dissipative wave pressure and a dissipative heating occurs (Isenberg & Hollweg 1982). Li & Li (2007, 2008) investigated effects due to interactions between ionized species for these non-Wentzel-Kramers-Brillouin (WKB) Alfvén waves. Further studies of multi-ion fluids on waves and anisotropic magnetic plasma instabilities have been carried out by Demars & Schunk (1979); Olsen & Leer (1999); Dzhililov et al. (2008). All these studies have been done analytically with simplifications or/and linear wave approximations.

Aside from solar physics, other fields have investigated multi-ion plasmas. Schunk (1977); Barakat & Schunk (1982) review the research on mixing multi-species in the anisotropic ionosphere and Ganguli (1996) in the polar magnetosphere (see also Demars & Schunk 1994). Echim et al. (2011); Abbo et al. (2016) review multi-fluids modeling and observations in the solar wind, and Krčička & Kubát (2000, 2001) in other stellar atmospheres. The latter two studies did not explicitly solve the equations describing magnetic field evolution. Other studies have shown the importance of including the induction equation (*e.g.*, Isenberg & Hollweg 1982; Martínez-Gómez et al. 2016) – the Larmor frequency of two different ionized species depends on the weighted atomic mass of the ionized atoms or molecules participating in the wave motion. Xie et al. (2004); Ofman et al. (2005) investigated wave dispersion in collisionless multi-ion plasmas. For this, they used nonlinear one-dimensional hybrid kinetic simulations of the multi-ion plasma to investigate high-frequency wave-particle interactions in the solar wind. Koch et al. (2005) found that measurements of the resonant frequency of the ion-

cyclotron wave can resolve the composition of the matter in the plasma, as the frequency depends on the abundances of the fluids comprising the plasma. They used the ElectroSpray Ionization Fourier Transform Ion Cyclotron Resonance Mass Spectrometry (ESI FT-ICR-MS) to reveal the composition of a dissolved organic matter, which was up to that point unknown.

In order to investigate the issues briefly presented above, we have developed the multi-fluid and multi-species (MFMS) numerical code: *Ebysus*. In the next section we briefly describe the physics implemented and numerical methods used in that code. Section 3 analyzes analytically the ionized multi-species coupling. We continue with investigating the importance of this coupling in the solar atmosphere using MHD models (Section 4). Our research includes the following numerical models (Section 5): 1D tests to validate the implementation (Section 5.1), and 1D numerical simulations including momentum exchange to investigate the dissipation of high-frequency standing waves (Section 5.2), 1D numerical simulations of high-frequency Alfvén waves (Sections 5.3). This manuscript ends with a discussion and conclusions (Section 6).

2. MULTI-FLUID AND MULTI-SPECIES MHD NUMERICAL CODE

We will dedicate a separate manuscript to a detailed description of the implementation and validation of the multi-fluid multi-species (MFMS) MHD equations used in *Ebysus* code. Therefore, for the purpose of this article, we limit ourselves to a short description of the code and the governing equations. *Ebysus* has inherited the numerical methods used in the *Bifrost* code (Gudiksen et al. 2011): Spatial derivatives and the interpolation of variables are done using sixth and fifth-order polynomials. As in *Bifrost*, the numerical scheme is defined on a staggered Cartesian mesh for which non-uniform grid spacing in one direction is allowed. The equations are stepped forward in time using the modified explicit third-order predictor-corrector procedure (Hyman et al. 1979) allowing variations in time and operator splitting. Numerical noise is suppressed using high-order artificial diffusion. In contrast to the *Bifrost* code, which solves the radiative-MHD equations for a single fluid, the *Ebysus* code solves the MHD equations separately for each of the desired number of excited levels, ionization stages, and species as detailed below. In addition, *Ebysus* takes into account the electron momentum equation through the induction equation and the derivation of the electric field and, independently, the electron energy equation.

For clarity and consistency we will use the same nomenclature as used by Ballester et al. (2018) with minor adjustments. The ionization states are referred as I , *i.e.*, $I = 0$ denotes neutrals and $\hat{I} = I \geq 1$ ions. The excited levels are marked with E and the identity of the chemical species (or molecules) is indi-

cated by a . Consequently, each set of particles in a given micro-state will be described with aIE . For electrons the notation aIE is reduced to just e . For simplicity, $\sum_{a'}$ is the sum over all the species a' , $\sum_{I',a}$ is the sum over all ionization levels, including neutrals, for a given species a and $\sum_{E',aI}$ is the sum over all the excited levels for a given ionized species aI . For clarity, we define $\sum_{a'I'E'} = \sum_{a'} \sum_{I',a'} \sum_{E',a'I'}$, and $\sum_{I'E',a} = \sum_{I',a} \sum_{E',aI'}$.

2.1. Continuity Equations

The mass density for each type of species in a given micro-state is governed by the continuity equation in this generic form:

$$\frac{\partial \rho_{aIE}}{\partial t} + \nabla \cdot \rho_{aIE} \vec{u}_{aIE} = \sum_{I'E',a} m_{aIE} (n_{aI'E'} \Gamma_{aI'E'/IE}^{ion} - n_{aIE} \Gamma_{aIEI'E'}^{rec}) \quad (1)$$

where $\rho_{aIE} = m_{aIE} n_{aIE}$, \vec{u}_{aIE} , n_{aIE} and m_{aIE} are the mass density, velocity, number density and particle mass for a given micro-state. $\Gamma_{aIEI'E'}^{rec}$, and $\Gamma_{aI'E'/IE}^{ion}$ are the transition rate coefficients between levels $I'E'$ and IE due to recombination or de-excitation, and ionization or excitation, respectively. The ionization, recombination, excitation and de-excitation terms have been added and are solved by applying a Newton-Raphson implicit method at each grid cell individually.

In this particular study, for simplicity, we neglect ionization and recombination. Our numerical experiments focus on the solar upper chromosphere and transition region, and the timescales modeled here are much shorter (≤ 1 s) than, for example, hydrogen ($\geq 10^2$ s) and helium ($10^3 - 10^5$ s) ionization and recombination timescales (Carlsson & Stein 1992, 2002; Golding et al. 2014). Non-equilibrium ionization effects for many heavier atoms occur on timescales of about 10-100 s for typical density values for transition region and corona (Smith & Hughes 2010). A detailed description of the ionization-recombination implementation and results will be detailed in upcoming studies.

Since electrons move so fast and their mass is negligible we ignore the continuity equation for electrons in the *Ebysus* code *i.e.*, we assume quasi-neutrality: $n_e = \sum_{aIE} n_{aIE} Z_{aI}$ where Z_{aI} is the ionized state. We denote the average velocity of the ionized species as $\vec{u}_c = \sum_{aIE} \vec{u}_{aIE}$ and of the neutrals as $\vec{u}_n = \sum_{a0E} \vec{u}_{a0E}$.

2.2. Momentum Equations

The momentum equations depend on the ionization state under consideration. The momentum equations for each aIE written in SI are included in the *Ebysus* code as follows:

$$\begin{aligned} & \frac{\partial(\rho_{aIE} \vec{u}_{aIE})}{\partial t} + \nabla \cdot (\rho_{aIE} \vec{u}_{aIE} \vec{u}_{aIE} - \hat{\tau}_{aIE}) = \\ & -\nabla P_{aIE} + \rho_{aIE} \vec{g} + n_{aIE} q_{aI} (\vec{E} + \vec{u}_{aIE} \times \vec{B}) + \\ & \sum_{I'E',a} (\Gamma_{aI'E'/IE}^{ion} m_{aIE} \vec{u}_{a0E'} - \Gamma_{aIEI'E'}^{rec} m_{aIE} \vec{u}_{aIE}) \\ & + \sum_{a'I'E'} \vec{R}_{aIE}^{aIEa'I'E'} \end{aligned} \quad (2)$$

$$\begin{aligned} & \frac{\partial(\rho_{a0E} \vec{u}_{a0E})}{\partial t} + \nabla \cdot (\rho_{a0E} \vec{u}_{a0E} - \hat{\tau}_{a0E}) = \\ & -\nabla P_{a0E} + \rho_{a0E} \vec{g} + \sum_{a'I'E'} \vec{R}_{a0E}^{a0Ea'I'E'} - \\ & \sum_{I'E',a} (\Gamma_{aI'E'}^{ion} m_{a0E} \vec{u}_{a0E} + \Gamma_{a0E}^{rec} m_{aI'E'} \vec{u}_{aI'E'}) \end{aligned} \quad (3)$$

where q_α , P_α , and $\hat{\tau}_\alpha$ are the ion charge, gas pressure, and viscous tensor for a specific species (*i.e.*, $\alpha = aIE$). \vec{g} , \vec{E} , and \vec{B} are gravity acceleration, and electric and magnetic field, respectively. $\vec{R}_\alpha^{\alpha\beta}$ is the momentum exchange where $\alpha \neq \beta$ and both can be any aIE . We combined charge and momentum exchange, *i.e.*, we summed both cross sections (Vranjes et al. 2008). Due to the numerical stiffness, the momentum exchange terms are solved by operator splitting; implicitly using a Newton-Raphson method along with the ionization/recombination terms in the continuity equation discussed above. The momentum exchange can then be expressed as follows:

$$\vec{R}_\alpha^{\alpha\beta} = m_\alpha n_\alpha \nu_{\alpha\beta} (\vec{u}_\beta - \vec{u}_\alpha) \quad (4)$$

where $\nu_{\alpha\beta}$ is the collision frequency. Note that $\vec{R}_\alpha^{\alpha\beta} = -\vec{R}_\beta^{\beta\alpha}$.

For neutral-ion and neutral-neutral, the collision frequencies ($\nu_{\alpha\beta}$) are typically expressed as follows:

$$\nu_{\alpha\beta} = n_\beta \frac{m_\beta}{m_\alpha + m_\beta} C_{\alpha\beta}(T_{\alpha\beta}) \sqrt{\frac{8K_B T_{\alpha\beta}}{\pi m_{\alpha\beta}}} \quad (5)$$

where the reduced temperature between the two fluids in K (see below) is $T_{\alpha\beta} = (m_\alpha T_\beta + m_\beta T_\alpha)/(m_\alpha + m_\beta)$ and $C_{\alpha\beta}(T_{\alpha\beta})$ is the cross section which is a function of temperature. Some relevant cross sections as a function of temperature are shown in (Krstic & Schultz 1999; Glassgold et al. 2005; Schultz et al. 2008; Vranjes et al. 2008; Vranjes & Krstic 2013, among others). We include both collisional momentum exchange and charge exchange. For those species where the cross section is not well-known we follow Vranjes et al. (2008), *i.e.*, the cross section between any other species with protons is chosen to be the value of the cross section for protons

multiplied by m_m/m_p , where m_m is the atomic mass of the considered species and m_p is the proton mass.

For elastic ion-ion collisions, we consider Coulomb collisions following, for instance, [Hansteen et al. \(1997\)](#). The collision frequency is as follows:

$$\nu_{a\hat{I}Ea'\hat{I}'E'} = 1.7 \frac{\ln \Lambda}{20} \frac{m_p}{m_{a\hat{I}E}} \left(\frac{m_{a\hat{I}Ea'\hat{I}'E'}}{m_p} \right)^{1/2} n_{a'\hat{I}'E'} T_{a\hat{I}Ea'\hat{I}'E'}^{-3/2} Z_{a'\hat{I}'}^2 Z_{a\hat{I}}^2 \quad (6)$$

where m_p is the proton mass, the collision frequency is measured in s^{-1} , and the ion number density in cm^{-3} , the reduced mass is $m_{a\hat{I}Ea'\hat{I}'E'} = \frac{m_{a\hat{I}E} m_{a'\hat{I}'E'}}{m_{a\hat{I}E} + m_{a'\hat{I}'E'}}$, and the Coulomb logarithm is (all in SI units).

$$\ln \Lambda = 23.0 + 1.5 \ln(T_e/10^6) - 0.5 \ln(n_e(cm^{-3})/10^6) \quad (7)$$

We ignore electron inertia and its time variation. We can then use the electron momentum equation to calculate the electric field (Section 2.5).

In addition to ionization and recombination, and to limit the scope of this study, to isolate and highlight effects of velocity drift between ions we highly simplified our approach in this study and we have also excluded the effects of gravity.

2.3. Energy Equations

The internal energy equations for each aIE implemented in the *Ebysus* code written in the SI conservative form are as follow:

$$\frac{\partial e_{a\hat{I}E}}{\partial t} = -\nabla \cdot e_{a\hat{I}E} \vec{u}_{a\hat{I}E} - P_{a\hat{I}E} \nabla \cdot \vec{u}_{a\hat{I}E} + Q_{a\hat{I}E}^{visc} + Q_{a\hat{I}E}^{ir} + Q_{a\hat{I}E}^{a\hat{I}Ee} + \sum_{a'I'E' \neq a\hat{I}E} Q_{a\hat{I}E}^{a\hat{I}Ea'I'E'} + q_{a\hat{I}E} n_{a\hat{I}E} \vec{u}_{a\hat{I}E} \cdot \vec{E} \quad (8)$$

$$\frac{\partial e_{a0E}}{\partial t} = -\nabla \cdot e_{a0E} \vec{u}_{a0E} - P_{a0E} \nabla \cdot \vec{u}_{a0E} + Q_{a0E}^{visc} + Q_{a0E}^{ir} + Q_{a0E}^{a0Ee} + \sum_{a'I'E' \neq a0E} Q_{a0E}^{a0Ea'I'E'} \quad (9)$$

$$\frac{\partial e_e}{\partial t} = -\nabla \cdot e_e \vec{u}_e - P_e \nabla \cdot \vec{u}_e + Q_e^{visc} + Q_e^{ir} + \sum_{a'I'E'} Q_e^{ea'I'E'} + q_e n_e \vec{u}_e \cdot \vec{E} + Q_{spitz} \quad (10)$$

where e_α is the internal energy for any $\alpha = [e, aIE]$. The last term in Equation 8 and the second last term in Equation 10 are the Joule heating. Q_α^{visc} is the viscous heating. Q_α^{ir} is the heating/cooling term due to the ionization, recombination excitation and/or de-excitation

energy exchange. $Q_\alpha^{\alpha\beta}$ is the heating of the fluid α due to collisions with fluid β for any $\alpha = [e, aIE]$ and $\beta = [e, a'I'E']$ as $Q_\alpha^{\alpha\beta} = \vec{R}_{\alpha\beta}^\alpha \cdot (\vec{u}_\beta - \vec{u}_\alpha)$. Q_{spitz} is the heating term due to thermal condition along the magnetic field. The latter is implemented using same scheme as in the *Bifrost* code. For simplicity and the purpose of the current paper, we do not take into account Q_{spitz} , Q_α^{ir} , $Q_e^{ea'I'E'}$, and Q_{aIE}^{aIEe} .

2.4. Equation of State

We assume MFMS ideal gases:

$$P_{aIE} = n_{aIE} k_B T_{aIE} = (\gamma - 1) e_{aIE} \quad (11)$$

i.e., each fluid/species has its own temperature and no internal degrees of freedom. As mentioned above, for this study, we are not taking into account the energies of ionization, recombination, excitation and de-excitation. Similarly, we need an equation of state for electrons:

$$P_e = n_e k_B T_e = (\gamma - 1) e_e, \quad (12)$$

where we assume quasi-neutrality to compute n_e .

2.5. Electric Field and the Induction Equation

The electric field can be defined in any reference system:

$$\vec{E} = \vec{E}_\alpha - \vec{u}_\alpha \times \vec{B} \quad (13)$$

In *Ebysus* we use the laboratory frame of reference – which in the case of the Sun means a frame of reference relative to the local solar conditions – and compute \vec{E}_α from the electron momentum equation (\vec{E}_e , *i.e.* electron frame of reference) which simplifies the implementation for the two-fluids, *i.e.*, ion and neutrals, or single fluid descriptions. Then \vec{E}_e is:

$$\vec{E}_e = \frac{\nabla P_e}{n_e q_e} + \frac{\sum_{aIE} \vec{R}_e^{eaIE}}{n_e q_e} \quad (14)$$

where all the inertia terms and the gravitational force acting on the electrons have been neglected. In addition, ionization/recombination is neglected, assuming the electron continuity equation is in the fast ionization/recombination limit.

The evolution of the magnetic field is governed by Maxwell equations. In *Ebysus*, we consider the induction equation:

$$\begin{aligned} \frac{\partial \vec{B}}{\partial t} &= -\nabla \times \vec{E} \\ &= \nabla \times \left(\vec{u}_e \times \vec{B} - \frac{\nabla P_e}{n_e q_e} - \frac{\sum_{aIE} \vec{R}_e^{eaIE}}{n_e q_e} \right) \end{aligned} \quad (15)$$

For simplicity and the purpose of this work, we do not take into account the electron pressure gradient term (the Biermann battery, the second term on the right hand side of the equation), nor the momentum exchange term between electrons and ion species (third term). Since we have several species, the electron velocity, thanks to the assumption of quasi-neutrality, reads as follows:

$$\vec{u}_e = \left(\sum_{\alpha} \frac{n_{\alpha} q_{\alpha} \vec{u}_{\alpha}}{n_e q_e} \right) - \frac{\vec{J}}{q_e n_e}, \quad (16)$$

and $\vec{J} = (\nabla \times \vec{B})/\mu_0$.

3. ANALYTICAL ANALYSIS

In this section, we describe analytically the coupling of ionized multi-species due to the electric field. First, we briefly describe the coupling in the momentum equation (Section 3.1). Second, how this coupling adds stiffness to the numerical code (Section 3.2) and finally we present an analytical solution (Section 3.3) in order to test the code (Section 5.1).

3.1. Coupling in the Momentum Equation for Ionized Species

The Lorentz force in a single fluid, or a two-fluids (ions and neutrals) description is $\vec{J} \times \vec{B}$. However, in full MFMS (Equation 2), the interaction of the Lorentz force with each ionized species reads as follows:

$$\begin{aligned} \frac{\partial \rho_{a\hat{i}E} u_{a\hat{i}E}}{\partial t} + = & -n_{a\hat{i}E} q_{a\hat{i}E} \\ & \left[\left(\sum_{a'\hat{i}E'} \frac{n_{a'\hat{i}E'} q_{a'\hat{i}E'} \vec{u}_{a'\hat{i}E'}}{n_e q_e} \right) - \right. \\ & \left. \frac{\vec{J}}{q_e n_e} - \vec{u}_{a\hat{i}E} \right] \times \vec{B} \end{aligned} \quad (17)$$

(*e.g.*, see Cramer 2001).

Observe, if $|\sum_{a'\hat{i}E'} n_{a'\hat{i}E'} q_{a'\hat{i}E'} \vec{u}_{a'\hat{i}E'} - n_e q_e \vec{u}_{a\hat{i}E}| \ll |\vec{J}|$ for any ionized element, the expression above becomes $\vec{J} \times \vec{B}$, which brings us back to single fluid or two-fluids nomenclature.

Note that the various momentum equations are coupled with the electric field as detailed with the Equations 17. The evolution of the velocity of an ionized species depends on the velocity of the other species as long as $|\sum_{a'\hat{i}E'} n_{a'\hat{i}E'} q_{a'\hat{i}E'} \vec{u}_{a'\hat{i}E'} - n_e q_e \vec{u}_{a\hat{i}E}|$ is large enough in relation to the other terms in the momentum equation. Collisions and ionization/recombination couple the momentum equations. We will focus on

cases where $|\sum_{a'\hat{i}E'} n_{a'\hat{i}E'} q_{a'\hat{i}E'} \vec{u}_{a'\hat{i}E'} - n_e q_e \vec{u}_{a\hat{i}E}|$ indeed may become important.

Let us define ion velocity drift *force* as follows:

$$\begin{aligned} \vec{F}_{a\hat{i}E}^{IDrift} = & -n_{a\hat{i}E} q_{a\hat{i}E} \\ & \left[\left(\sum_{a'\hat{i}E'} \frac{n_{a'\hat{i}E'} q_{a'\hat{i}E'} \vec{u}_{a'\hat{i}E'}}{n_e q_e} \right) - \vec{u}_{a\hat{i}E} \right] \times \vec{B} \\ = & \frac{n_{a\hat{i}E} q_{a\hat{i}E}}{n_e q_e} \\ & \left[\sum_{a'\hat{i}E' \neq a\hat{i}E} n_{a'\hat{i}E'} q_{a'\hat{i}E'} (\vec{u}_{a\hat{i}E} - \vec{u}_{a'\hat{i}E'}) \right] \times \vec{B} \end{aligned} \quad (18)$$

i.e., $\vec{J} \times \vec{B}$ has been subtracted. This term is not zero when two or more ionized species move at different velocities. Another interesting aspect is that this term does not appear in the induction equation since the electric field is a function of the bulk velocity of all ions (Equation 16) and changes in the velocity due to F^{IDrift} will not impact the electric field.

Because of the coupling due to the velocity drift force, ions can experience a synchronized cyclotron type motion. In other words, when several species are present with different velocities, they will be coupled to the other ionized species and will experience (as shown in the next section) a rotational motion with a frequency that depends on a combination of single-ion cyclotron-frequencies, the number density of ionized species and their ionization state (as detailed below; similarly Martínez-Gómez et al. 2016, derived this expression). For two ionized species, this coupling leads to a multi-ion cyclotron frequency:

$$\hat{\Omega}_{a\hat{i}Ea'\hat{i}E'} = \frac{Z_{a\hat{i}} n_{a\hat{i}E} \Omega_{a'\hat{i}E'} + Z_{a'\hat{i}} n_{a'\hat{i}E'} \Omega_{a\hat{i}E}}{n_e} \quad (19)$$

where the cyclotron frequency for a specific species is $\Omega_{a\hat{i}E} = \frac{q_{a\hat{i}} |\vec{B}|}{m_{a\hat{i}E}}$ (see Section 3.3). By increasing the number of ionized species, the number of superpositions of multi-ion cyclotron frequencies increases. The multi-ion cyclotron frequency becomes a combination of the cyclotron frequencies of the ionized species (Section 5.1).

3.2. CFL

The ion velocity drift force adds a new Courant Friedrichs and Lewy (CFL) convergence condition (Courant et al. 1928) for MFMS MHD equations due to the multi-ion cyclotron frequencies. Consequently, the length of a timestep cannot be greater than $1/\hat{\Omega}_{a\hat{i}Ea'\hat{i}E'}$, and this condition has to be fulfilled for each coupling between ionized species, considering the largest $\hat{\Omega}_{a\hat{i}Ea'\hat{i}E'}$.

3.3. An Analytic Solution

In this section, following [Cramer \(2001\)](#), we derive the analytic formulation of the multi-ion cyclotron wave in simplified conditions without the effects of ionization and recombination, radiative losses, thermal conduction, the Hall term, Biermann battery, nor momentum exchange and gravity. We use that solution to validate our numerical experiments.

In an atmosphere with no spatial variation in any of the thermal and density variables for any of the micro-states aIE , and given a constant magnetic field, *i.e.*, $\vec{J} = 0$, the multi-fluid momentum equations can be simplified to:

$$\frac{\partial \vec{u}_{a\hat{I}E}}{\partial t} = \frac{q_{a\hat{I}E}}{m_{a\hat{I}E} n_e q_e} \left[\sum_{a'\hat{I}'E' \neq a\hat{I}E} n_{a'\hat{I}'E'} q_{a'\hat{I}'E'} (\vec{u}_{a\hat{I}E} - \vec{u}_{a'\hat{I}'E'}) \right] \times \vec{B} \quad (20)$$

The magnetic field does not change in time $\frac{\partial \vec{B}}{\partial t} = 0$ because we imposed $\vec{J} = 0$ and the bulk velocity and density are constant in space. This set of equations has as a solution a superposition of sinusoids, as we show below. For simplicity, let us consider only two singly-ionized fluids, *e.g.*, H^+ and He^+ . Since we allow only singly ionized species, *i.e.*, $q_e = q_{H^+} = q_{He^+}$, and $n_e = n_{H^+} + n_{He^+}$, then:

$$\frac{\partial \vec{u}_{H^+}}{\partial t} = \frac{q_e n_{He^+}}{m_{H^+}} \left[\frac{\vec{u}_{H^+} - \vec{u}_{He^+}}{n_{H^+} + n_{He^+}} \right] \times \vec{B} \quad (21)$$

$$\frac{\partial \vec{u}_{He^+}}{\partial t} = \frac{q_e n_{H^+}}{m_{He^+}} \left[\frac{\vec{u}_{He^+} - \vec{u}_{H^+}}{n_{H^+} + n_{He^+}} \right] \times \vec{B} \quad (22)$$

Note that the acceleration of a particular species depends on the particle mass of that species and on the number density of the other ionized species. The larger the number density from one species the larger the acceleration for the other species. These two equations can be combined in order to derive the evolution of the velocity drift ($\vec{u}_{D_{H^+He^+}} = \vec{u}_{H^+} - \vec{u}_{He^+}$).

$$\frac{\partial \vec{u}_{D_{H^+He^+}}}{\partial t} = \frac{q_e}{n_e} \left[\frac{n_{He^+}}{m_{H^+}} \vec{u}_{D_{H^+He^+}} + \frac{n_{H^+}}{m_{He^+}} \vec{u}_{D_{H^+He^+}} \right] \times \vec{B} \quad (23)$$

For a velocity drift perpendicular to the magnetic field (for instance, within the x-z plane and the magnetic field is aligned with the y-axis) the equations can be reduced to:

$$\frac{\partial u_{D_{x_{H^+He^+}}}}{\partial t} = -\frac{q_e}{n_e} \left[\frac{n_{He^+}}{m_{H^+}} + \frac{n_{H^+}}{m_{He^+}} \right] u_{D_{z_{H^+He^+}}} B_y \quad (24)$$

$$\frac{\partial u_{D_{z_{H^+He^+}}}}{\partial t} = \frac{q_e}{n_e} \left[\frac{n_{He^+}}{m_{H^+}} + \frac{n_{H^+}}{m_{He^+}} \right] u_{D_{x_{H^+He^+}}} B_y \quad (25)$$

One can decompose these equations into a wave-like form:

$$u_{D_{x_{H^+He^+}}} = U_D^o \sin \left(\frac{q_e}{n_e} \left[\frac{n_{He^+}}{m_{H^+}} + \frac{n_{H^+}}{m_{He^+}} \right] B_y t \right) \quad (26)$$

$$u_{D_{z_{H^+He^+}}} = -U_D^o \cos \left(\frac{q_e}{n_e} \left[\frac{n_{He^+}}{m_{H^+}} + \frac{n_{H^+}}{m_{He^+}} \right] B_y t \right) \quad (27)$$

where U_D^o is the absolute initial ion velocity drift. This simple solution can be used to test the numerical implementation (Section 5.1). The generic solution for many ionized species is a complex combination of velocity drifts and not Equation 19. The number of superposition sinusoidal functions will increase with number of ionized levels and species and these frequencies depend on the atomic mass, magnetic field strength, charge and number density for each ionized micro-state and electron number density.

4. IMPORTANCE OF THE MULTI-SPECIES IN THE SOLAR ATMOSPHERE

In order to better understand how important multi-fluid and multi-species effects are in the solar atmosphere, we use in this section the time-dependent 2.5D radiative MHD numerical model by [Martinez-Sykora et al. \(2019\)](#) calculated with the *Bifrost* code. This model solves the hydrogen and helium rate equations including non-equilibrium ionization ([Leenaarts et al. 2007](#); [Golding et al. 2016](#)) and ion-neutral interaction effects introduced through Generalized Ohm's Law ([Martínez-Sykora et al. 2012, 2017a](#); [Nóbrega-Siverio et al. 2020a](#)). The numerical domain spans from the upper layers of the convection zone, through the photosphere, chromosphere and transition region, to the corona. The advantage of using this model is that it aims to replicate more realistic conditions than we can for now with the *Ebysus* code, thus allowing insight into typical parameters of the solar atmosphere that can be used for *Ebysus* studies. Figure 1 shows temperature, density and magnetic field strength maps, revealing low lying transition loops, magneto-acoustic shocks as well as two types of spicules, and including a million degrees corona. The magnetic field configuration is designed to mimic a plage region (for further details, see [Martinez-Sykora et al. 2019](#)).

4.1. From a Collisional to a Collisionless Multi-species Solar Atmosphere

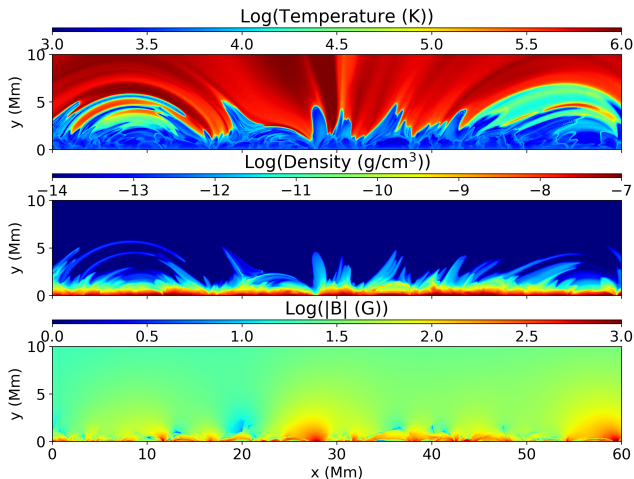


Figure 1. We use [Martinez-Sykora et al. \(2019\)](#)’s 2.5D radiative MHD simulation to investigate the importance of the ion cyclotron resonance described in the previous section. From top to bottom, temperature, density and absolute magnetic field strength maps are shown for the selected instant in the simulated timeseries.

The solar atmosphere has a highly complex chemical composition (*e.g.*, [Asplund et al. 2009](#)). As long as the collision frequencies between species which constitute solar plasma are slow compared with other relevant physical processes, multi-species interaction effects must be taken into account.

We have estimated various collision frequencies from [Martinez-Sykora et al. \(2019\)](#)’s time-dependent 2.5D radiative MHD simulation. $H^+ - He^+$, $H^+ - He^{++}$, $He^+ - He^{++}$, $H^+ - i$, $He^+ - i$, $H^+ - n$, and $He^+ - n$ collision frequencies are shown in Figure 2 from top to bottom respectively. The estimated collision frequencies between H^+ or He^+ with ions in the upper chromosphere and transition region ranges from a few 1 Hz to 10^3 Hz. For the processes of interest in this paper, we will show that thermo-dynamic timescales can be shorter and the multi-species interaction effects can become relevant in upper chromosphere, TR and lower corona.

4.2. Weighted Averaged Ion-cyclotron Frequencies and Collisions: Upper Chromosphere and TR

It is thus of great interest to compare the collisions frequencies between different ionized species and the multi-ion cyclotron frequencies. Using the [Martinez-Sykora et al. \(2019\)](#) 2.5D radiative MHD simulation, we also calculated the multi-ion cyclotron frequencies between $H^+ - He^+$, $H^+ - He^{++}$, and $He^+ - He^{++}$ using expression 19 (from top to bottom in Figure 3). For $H^+ - He^+$ and $H^+ - He^{++}$, these multi-ion cyclotron frequencies are high, ranging from 10^2 to 10^6 Hz. Within the chromosphere, they become smaller (ranging from 10 to 10^4 Hz) in cold regions (yellow areas in top two panels near $z=0.5$ Mm).

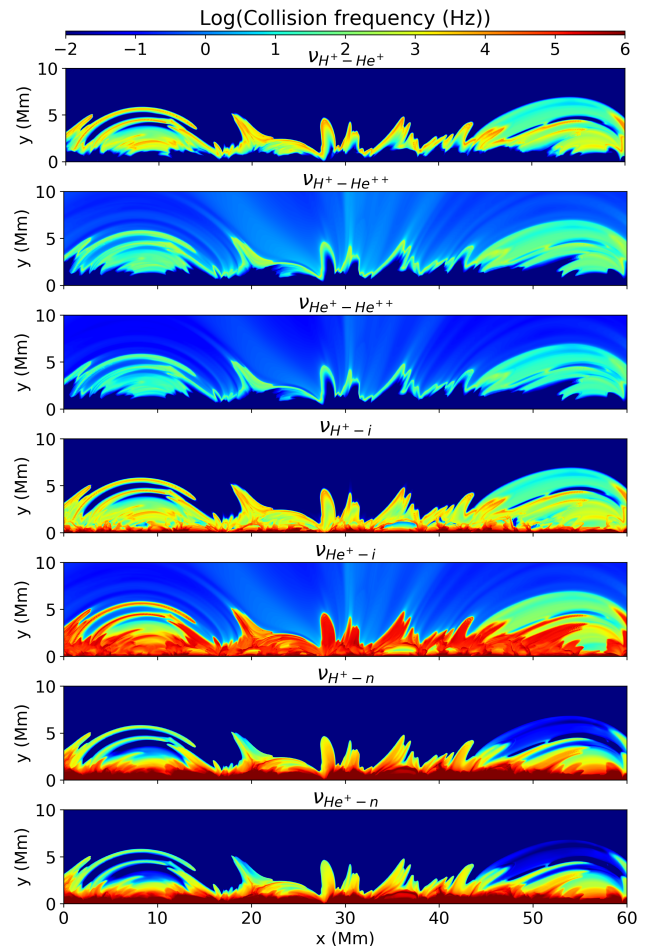


Figure 2. The collision frequency between different ionized species is small in the upper chromosphere, transition region and corona. $H^+ - He^+$, $H^+ - He^{++}$, $He^+ - He^{++}$, $H^+ - i$, $He^+ - i$, $H^+ - n$, and $He^+ - n$ collision frequencies are shown from top to bottom. Ions (i) and neutrals (n) include the sixteen top most abundant species.

The lowest multi-ion cyclotron frequencies are for $He^+ - He^{++}$ (from 1 to 10^4 Hz).

The velocity drift between the different ionized species, or the multi-ion cyclotron wave amplitudes, can be reduced by collisions between species. Taking into account the analysis from the previous section, the collision frequency between different ionized species is very small in the upper chromosphere, transition region and corona. Typical collisional chromospheric timescales are of the order of a fraction of second (which frequency is $\simeq 1$ Hz). Figure 4 compares collision frequencies with multi-ion cyclotron frequencies. In the lower chromosphere and below, the multi-ion cyclotron frequency is much lower than the collision frequencies. Consequently, collisions will not allow the production of ion-cyclotron waves. In the corona, collisions are much less frequent and thus cannot significantly alter these waves. From

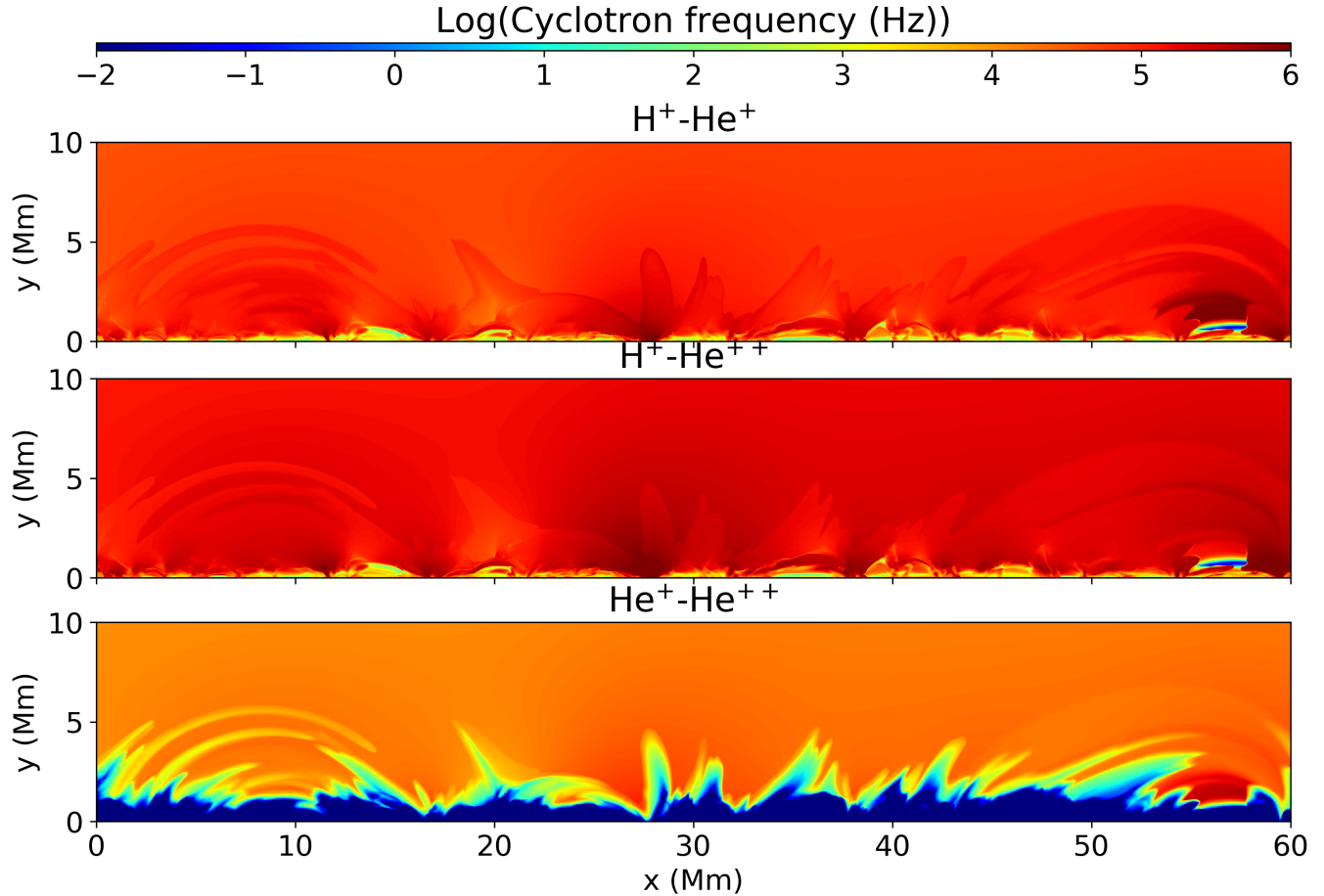


Figure 3. The multi-ion cyclotron frequencies frequency is high in the upper chromosphere and corona. The multi-ion cyclotron frequency between ionized hydrogen and singly ionized helium level, ionized hydrogen and double ionized helium level, and singly ionized helium level and double ionized helium level are shown from top to bottom.

the mid-chromosphere to the transition region multi-ion cyclotron waves can become important for interactions between H^+-He^+ and H^+-He^{++} , and for He^+-He^{++} in the transition region. These regions of interest includes spicules, low laying loops and dynamic fibrils. In these regions where the collisions are comparable to the multi-ion cyclotron frequencies, these waves can be generated, propagate over a certain distance, and be dissipated through collisions. In Section 5.3 we show that Alfvén waves can generate ion-velocity drifts and this means that collisions can provide an efficient mechanism for dissipation of high-frequency Alfvén waves (Martínez-Gómez et al. 2016).

In the single fluid description, even when including ion-neutral interaction effects (*e.g.*, ambipolar or Pedersen diffusion), or for a two-fluid description such as ions and neutrals or ions and electrons, we impose the same velocity for all species, and all ionized species ($a\hat{I}E$) move at the same speed. The same is true for all neutral species ($a0E$). Consequently, these simplified descriptions implicitly assume that 1) forces acting on each

$a\hat{I}E$ and on each $a0E$ should be the same 2) the collisional time-scales must be small enough 3) and drivers must act on time-scales larger than the multi-ion cyclotron frequencies, *i.e.*, velocity drifts between species must be negligible compared to bulk ionized plasma velocity. However, as we show in the above, in the solar atmosphere these conditions likely do not always apply. For example, the forces acting on each aIE are not always the same, since each aIE may have a different mass and ionization state. In addition, as we have shown in this section, the collision frequency between different ionized species is very small in the upper chromosphere, transition region and corona, and therefore the velocity drift between ionized species may not be damped by collisions.

5. NUMERICAL EXPERIMENTS

Of all the various physical processes that *Ebysus* is capable of handling, we here only use a subset. The main subject of the current work is to study and isolate the electric force (F^{IDrift}) due to ion drift velocities, which

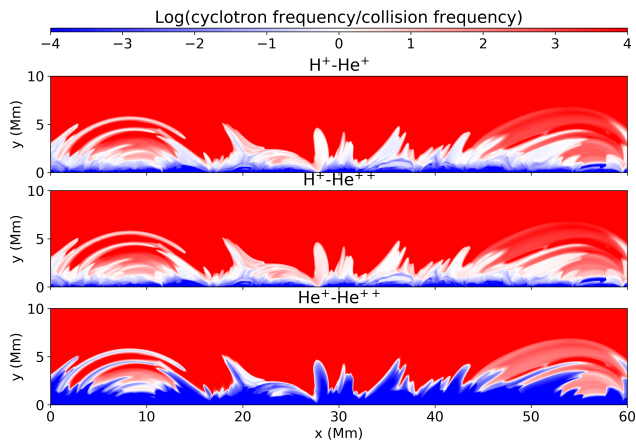


Figure 4. The multi-ion cyclotron waves will facilitate the dissipation of Alfvénic waves in the chromosphere and TR. Ratio between these cyclotron frequencies with the collision frequencies between ionized hydrogen and first ionized helium level, ionized hydrogen and second ionized helium level, and first ionized helium level and second ionized helium level are shown from top to bottom.

is the main subject of this work. As mentioned above, neither gravity, ionization and recombination, the Hall term, the Biermann battery, radiative losses, nor thermal conduction are taken into account here.

First, we analyze three sets of 1D numerical simulations (Section 5.1). The first set of 1D numerical tests is used to compare the codes’ implementation with the analytic solution described in Section 3.3. The second set of 1D numerical models focuses on the possible role of the ion-velocity drift in the upper chromospheric thermodynamics (Section 5.2). The last set of 1D numerical models is focused on multi-ion cyclotron waves driven by Alfvén waves (Section 5.3). Table 1 summarizes these experiments with the list of species included in each of the experiments along with relevant initial and/or boundary conditions.

5.1. 1D Collisionless Numerical Experiments

The 1.5D collisionless numerical experiments of multi-ion cyclotron standing waves shown here validates the numerical implementation used in *Ebysus* by comparison with the analytical solutions described in Section 3.3.

The numerical domain in all 1.5D numerical experiments shown here are set up along the z -axis and cover the range $z = [0, 1]$ Mm with a uniform grid of 200 points. Boundaries are periodic. The constant magnetic field is perpendicular to the simulated numerical domain, and is oriented along the y -axis. We impose an initial velocity along the z -axis, perpendicular to the magnetic field. Note that the ion-cyclotron frequency is independent of the internal energy and the thermodynamic properties of neutral species (see Equation 19).

Figure 5 shows the various velocity components for each ionized species as a function of time for experiment 1D2S2LNI. This experiment includes two species, *i.e.*, hydrogen and helium, with two levels each: neutrals and single ionized ions (Table 1). The magneto-thermal properties are constant with a magnetic field strength of $B_y = 1$ G. Note that these preliminary models are meant to validate the implementation and we choose low magnetic field strengths in order to avoid prohibitively small timesteps. Other initial thermodynamic properties of the simulations are listed in Table 2. Figure 5 shows that the cyclotron motion is coupled between ionized hydrogen and ionized helium due to the electric field (Equation 17). The analytic solution (Equation 19) for 1D2S2LNI provides a frequency of 62 Hz, for all ionized species and velocity components in agreement with the numerical experiments. The different components (x and z) of the velocities of ionized species are 90 degrees out of phase, *i.e.*, they rotate. In addition, the velocities of the two ionized species are in anti-phase as expected from Equations 21-27. The velocity amplitude is larger for He^+ because, as mentioned above, the acceleration depends on its own particle mass and the number of particles of the other species. Since He^+ weighs more than H^+ , this reduces the accelerations in He^+ , but since n_{H^+} is much larger than n_{He^+} , the acceleration is larger in He^+ than in H^+ .

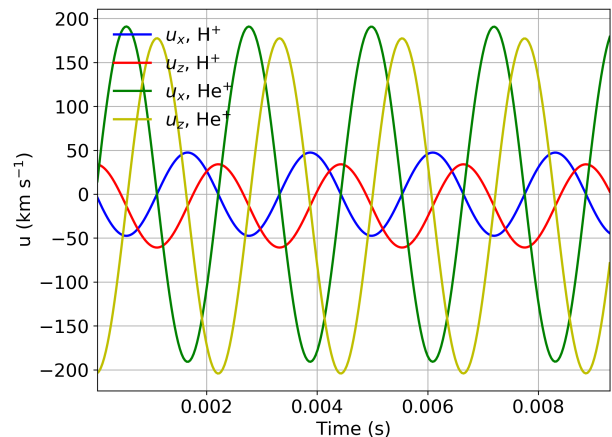


Figure 5. Note that the various components of the velocity for any ionized species and levels have the same frequency. Component x and z of the velocity as a function of time for the various ionized species (see labels) are shown for simulation 1D2S2LNI.

As mentioned above, adding new ionized species will add wave superposition with different frequencies and amplitudes. Note that Equation 19 is only valid for two ionized species. Figure 6 shows the various velocity components for the ionized species of simulation 1D3S2LNI which includes three species (hydrogen, helium and carbon) with two levels each (Table 1). Table 2 provides

Table 1. List of numerical simulations. From left to right: list the name, type of species and number of ionized levels and other properties of the simulated domain.

Name	aI	Other properties
1D2S2LNI	H:2 lvl, He:2 lvl	Collisionless and initial ion velocity drift
1D3S2LNI	H:2 lvl, He:2 lvl, C:2 lvl	Collisionless and initial ion velocity drift
1D2S2LCI	H:2 lvl, He:2 lvl	Collisional and initial ion velocity drift
1D2S2LB0	H:2 lvl, He:2 lvl	Collisionless & boundary driven (0.1 Hz)
1D2S2LB1	H:2 lvl, He:2 lvl	Collisionless & boundary driven (10 Hz, $\Delta B_x = 0.25$ G)
1D2S2LB2	H:2 lvl, He:2 lvl	Collisionless & boundary driven (20 Hz, $\Delta B_x = 0.25$ G)
1D2S2LB3	H:2 lvl, He:2 lvl	Collisionless & boundary driven (10^2 Hz, $\Delta B_x = 0.25$ G)
1D2S2LB4	H:2 lvl, He:2 lvl	Collisionless & boundary driven (200 Hz, $\Delta B_x = 0.25$ G)
1D2S2LB5	H:2 lvl, He:2 lvl	Collisionless & boundary driven (10^3 Hz, $\Delta B_x = 0.25$ G)
1D2S2LB6	H:2 lvl, He:2 lvl	Collisionless & boundary driven (10^5 Hz, $\Delta B_x = 0.25$ G)
1D2S2LB7	H:2 lvl, He:2 lvl	Collisionless & boundary driven (10^3 Hz, $\Delta B_x = 0.025$ G)
1D2S2LB8	H:2 lvl, He:2 lvl	Collisionless & boundary driven (10^3 Hz, $\Delta B_x = 2.5$ G)

densities for each species and levels. H and He follow photospheric abundances. In order to have enough ionized C, we increased the density and, therefore, the abundance with respect to the photospheric abundance in order to illustrate complex coupling since the various multi-ion cyclotron depend on the density number of each ionized species (*e.g.*, Equations 26-27). Otherwise, since the amplitude on these multi-ion frequencies dependent on the density, C contribution will be negligible. The multi-ion cyclotron frequency is not as trivial to derive as for two ionized species (Section 3.3) and becomes a combination of the cyclotron frequency of the various ionized species. With three different ionized species one can discern two different multi-ion cyclotron frequencies in Figure 6. In short, number densities, atomic mass, field strength and charge play a role in the amplitudes and frequencies as described above and following Equations 21-27 (see also Martínez-Gómez et al. 2016).

5.2. Kinetic Energy Dissipation

Momentum exchange between species could dissipate any multi-ion cyclotron waves that may occur in the upper chromosphere, TR and lower corona (Figure 3). Let us investigate if such dissipation can heat the solar atmosphere. Experiment 1D2S2LCI has typical upper-chromosphere/transition region densities and energies (Table 2). The simulated atmosphere is uniform and includes hydrogen and helium with two levels each (neutrals and first ionization level, Table 1). This numerical experiment includes momentum exchange. The top and middle panels of Figure 7 show the x and z components of the velocity, respectively, and the bottom panel the temperature for each level of each species. The amplitude of the multi-ion cyclotron wave is damped by a factor e due to momentum exchange in roughly $3 \cdot 10^{-4}$ s. Note that neutrals also show temperature variations in

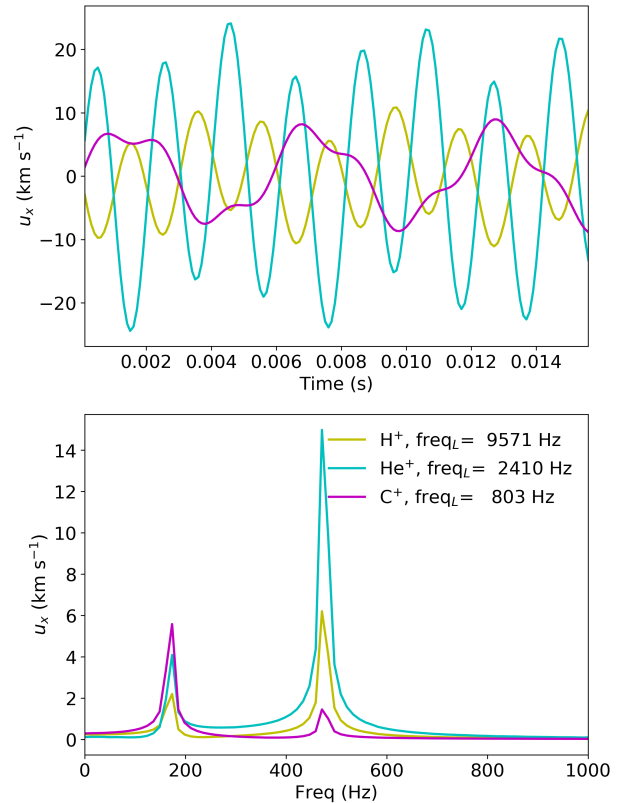


Figure 6. Component x of the velocity as a function of time (top) and frequency (bottom) for the various species, hydrogen, helium, and carbon, for their ionized level (see labels) for simulation 1D3S2LNI. For comparison, we have added the relevant Lamor frequencies to the labels.

time due to the momentum transfer from the ions. This dissipation heats the corresponding level of each species following:

ION DRIFT IN THE SOLAR ATMOSPHERE

ID	ρ_{H^0}	n_{H^0}	ρ_{H^+}	n_{H^+}	ρ_{He^0}	n_{He^0}	ρ_{He^+}	n_{He^+}	ρ_{C^0}	n_{C^0}	ρ_{C^+}	n_{H^0}
ID2S2LNI	$1.4 \cdot 10^{-10}$	$8.5 \cdot 10^{13}$	$5.8 \cdot 10^{-10}$	$3.5 \cdot 10^{14}$	$1.4 \cdot 10^{-10}$	$2.2 \cdot 10^{13}$	$1.4 \cdot 10^{-10}$	$2.2 \cdot 10^{13}$	N/A	N/A	N/A	N/A
ID3S2LNI	$3 \cdot 10^{-9}$	$1.8 \cdot 10^{15}$	$4 \cdot 10^{-9}$	$2.4 \cdot 10^{15}$	$1.4 \cdot 10^{-9}$	$2.1 \cdot 10^{14}$	$1.4 \cdot 10^{-9}$	$2.1 \cdot 10^{14}$	$6.6 \cdot 10^{-11}$	$3.3 \cdot 10^{12}$	$2.6 \cdot 10^{-9}$	$1.3 \cdot 10^{14}$
ID2S2LCI	$4 \cdot 10^{-17}$	$2.7 \cdot 10^7$	$7.3 \cdot 10^{-14}$	$4.4 \cdot 10^{10}$	$6.5 \cdot 10^{-15}$	$0.8 \cdot 10^8$	$1.8 \cdot 10^{-14}$	$2.8 \cdot 10^9$	N/A	N/A	N/A	N/A
ID2S2LB0	$2 \cdot 10^{-19}$	$1.3 \cdot 10^5$	$7.2 \cdot 10^{-13}$	$4.3 \cdot 10^{11}$	$2.9 \cdot 10^{-15}$	$4.3 \cdot 10^8$	$2.9 \cdot 10^{-13}$	$4.3 \cdot 10^{10}$	N/A	N/A	N/A	N/A
ID2S2LB1	$2 \cdot 10^{-19}$	$1.3 \cdot 10^5$	$7.2 \cdot 10^{-13}$	$4.3 \cdot 10^{11}$	$2.9 \cdot 10^{-15}$	$4.3 \cdot 10^8$	$2.9 \cdot 10^{-13}$	$4.3 \cdot 10^{10}$	N/A	N/A	N/A	N/A
ID2S2LB2	$2 \cdot 10^{-19}$	$1.3 \cdot 10^5$	$7.2 \cdot 10^{-13}$	$4.3 \cdot 10^{11}$	$2.9 \cdot 10^{-15}$	$4.3 \cdot 10^8$	$2.9 \cdot 10^{-13}$	$4.3 \cdot 10^{10}$	N/A	N/A	N/A	N/A
ID2S2LB3	$2 \cdot 10^{-19}$	$1.3 \cdot 10^5$	$7.2 \cdot 10^{-13}$	$4.3 \cdot 10^{11}$	$2.9 \cdot 10^{-15}$	$4.3 \cdot 10^8$	$2.9 \cdot 10^{-13}$	$4.3 \cdot 10^{10}$	N/A	N/A	N/A	N/A
ID2S2LB4	$2 \cdot 10^{-19}$	$1.3 \cdot 10^5$	$7.2 \cdot 10^{-13}$	$4.3 \cdot 10^{11}$	$2.9 \cdot 10^{-15}$	$4.3 \cdot 10^8$	$2.9 \cdot 10^{-13}$	$4.3 \cdot 10^{10}$	N/A	N/A	N/A	N/A
ID2S2LB5	$2 \cdot 10^{-19}$	$1.3 \cdot 10^5$	$7.2 \cdot 10^{-13}$	$4.3 \cdot 10^{11}$	$2.9 \cdot 10^{-15}$	$4.3 \cdot 10^8$	$2.9 \cdot 10^{-13}$	$4.3 \cdot 10^{10}$	N/A	N/A	N/A	N/A
ID2S2LB6	$2 \cdot 10^{-19}$	$1.3 \cdot 10^5$	$7.2 \cdot 10^{-13}$	$4.3 \cdot 10^{11}$	$2.9 \cdot 10^{-15}$	$4.3 \cdot 10^8$	$2.9 \cdot 10^{-13}$	$4.3 \cdot 10^{10}$	N/A	N/A	N/A	N/A
ID2S2LB7	$2 \cdot 10^{-19}$	$1.3 \cdot 10^5$	$7.2 \cdot 10^{-13}$	$4.3 \cdot 10^{11}$	$2.9 \cdot 10^{-15}$	$4.3 \cdot 10^8$	$2.9 \cdot 10^{-13}$	$4.3 \cdot 10^{10}$	N/A	N/A	N/A	N/A
ID2S2LB8	$2 \cdot 10^{-19}$	$1.3 \cdot 10^5$	$7.2 \cdot 10^{-13}$	$4.3 \cdot 10^{11}$	$2.9 \cdot 10^{-15}$	$4.3 \cdot 10^8$	$2.9 \cdot 10^{-13}$	$4.3 \cdot 10^{10}$	N/A	N/A	N/A	N/A
ID	$u_{\text{H}^+}^-$	$u_{\text{H}^+}^+$	$u_{\text{C}^+}^-$	T	\vec{B}	v_a	dz	nz				
ID2S2LNI	(-3.6, 0, 34)	(14, 0, -200)	N/A	10^4	(0, 1, 0)	0.02	5	200				
ID3S2LNI	(-2.9, 0, 4.5)	(5.7, 0, -20)	1.4, -15	10^4	(0, 1, 0)	0.08	5	200				
ID2S2LCI	(-4.3, 0, 0.04)	(-9.3, 0, 2.2)	N/A	$4 \cdot 10^4$	(0, 10, 0)	90	100	200				
ID2S2LB0	(0, 0, 0)	(0, 0, 0)	N/A	$4 \cdot 10^4$	(0, 0, 10)	28	10^{-2}	2000				
ID2S2LB1	(0, 0, 0)	(0, 0, 0)	N/A	$4 \cdot 10^4$	(0, 0, 10)	28	$1.2 \cdot 10^{-2}$	2000				
ID2S2LB2	(0, 0, 0)	(0, 0, 0)	N/A	$4 \cdot 10^4$	(0, 0, 10)	28	$6 \cdot 10^{-3}$	2000				
ID2S2LB3	(0, 0, 0)	(0, 0, 0)	N/A	$4 \cdot 10^4$	(0, 0, 10)	28	$2 \cdot 10^{-3}$	2000				
ID2S2LB4	(0, 0, 0)	(0, 0, 0)	N/A	$4 \cdot 10^4$	(0, 0, 10)	28	10^{-3}	2000				
ID2S2LB5	(0, 0, 0)	(0, 0, 0)	N/A	$4 \cdot 10^4$	(0, 0, 10)	28	$2 \cdot 10^{-4}$	2000				
ID2S2LB6	(0, 0, 0)	(0, 0, 0)	N/A	$4 \cdot 10^4$	(0, 0, 10)	28	$3 \cdot 10^{-6}$	2000				
ID2S2LB7	(0, 0, 0)	(0, 0, 0)	N/A	$4 \cdot 10^4$	(0, 0, 10)	28	$2 \cdot 10^{-4}$	2000				
ID2S2LB8	(0, 0, 0)	(0, 0, 0)	N/A	$4 \cdot 10^4$	(0, 0, 10)	28	$2 \cdot 10^{-4}$	2000				

Table 2. Initial thermodynamic properties of the ID numerical simulations. Left to right: mass density (g cm^{-3}), number density (cm^{-3}), initial velocity (km s^{-1}) for H^+ , He^+ , and C^+ , temperature (K), magnetic field (G), Alfvén speed (km s^{-1}), grid spacing (km) and number of grid points. All experiments have velocities 0 km s^{-1} for neutrals.

$$Q_{\alpha}^{\alpha\beta} = R_{\alpha}^{\alpha\beta} \cdot (\vec{u}_{\alpha} - \vec{u}_{\beta}) \quad (28)$$

Since He^+ initially has the largest amplitude and the lowest solar number densities, it reaches the highest temperatures. Due to collisions, the plasma is not only heated but the temperatures of all species converge following:

$$Q_{\alpha}^{\alpha\beta} = 3 \frac{m_{\alpha\beta}}{m_{\alpha}} n_{\alpha} \nu_{\alpha\beta} k_B (T_{\beta} - T_{\alpha}) \quad (29)$$

So, in this case the helium is heated first through dissipation of the drift velocities, and then helium heats the other species and fluids. The time needed for the different species of the plasma to reach similar temperatures is larger than the time needed to damp the multi-ion cyclotron wave and this depends on the heating as well the density. The coupling between the different fluids is different. For instance, neutral hydrogen is more coupled to the ions than neutral helium is due to their different cross-sections as well as the densities of the different fluids (Figure 2). For the lower densities of the upper transition region or corona, the damping time-scales increase by an order of magnitude or more.

Consequently, if these multi-ion cyclotron waves (or velocity drift between ionized species) can be generated, this may be an effective dissipation and heating mechanism for the plasma in the upper chromosphere and TR and lower corona. Therefore, it is of great interest to investigate which mechanisms could lead to the formation of such waves and how much energy is contained in such high-frequency modes. Current MHD models do not include the physics of these drift velocities, neither their generation or their dissipation.

5.3. Alfvén Waves

The equations and analysis in detailed in Section 3.3 suggest that magnetic tension, such as the restoring force in Alfvén waves, may lead to ion velocity drifts. Martínez-Gómez et al. (2016) analytical analysis from multi-fluid and multi-species studies show that in order to generate waves at the multi-ion cyclotron frequencies, the Alfvén frequency must be the same or greater than those frequencies. We performed seven 1D simulations driving Alfvén waves of differing frequencies at the bottom boundary (Table 1). For the 1D2S2LB0, 1D2S2LB1, 1D2S2LB2, 1D2S2LB3, 1D2S2LB4, 1D2S2LB5, and 1D2S2LB6 simulations Alfvén waves are driven at frequencies of 0.1, 10, 20, 10^2 , 200, 10^3 and 10^5 Hz, respectively, which except for simulation 1D2S2LB6 are all smaller than the multi-ion cyclotron frequency ($1.5 \cdot 10^4$ Hz). In all these experiments, in order to drive the Alfvén wave, we impose a background magnetic field with an initial $B_z = 10$ G.

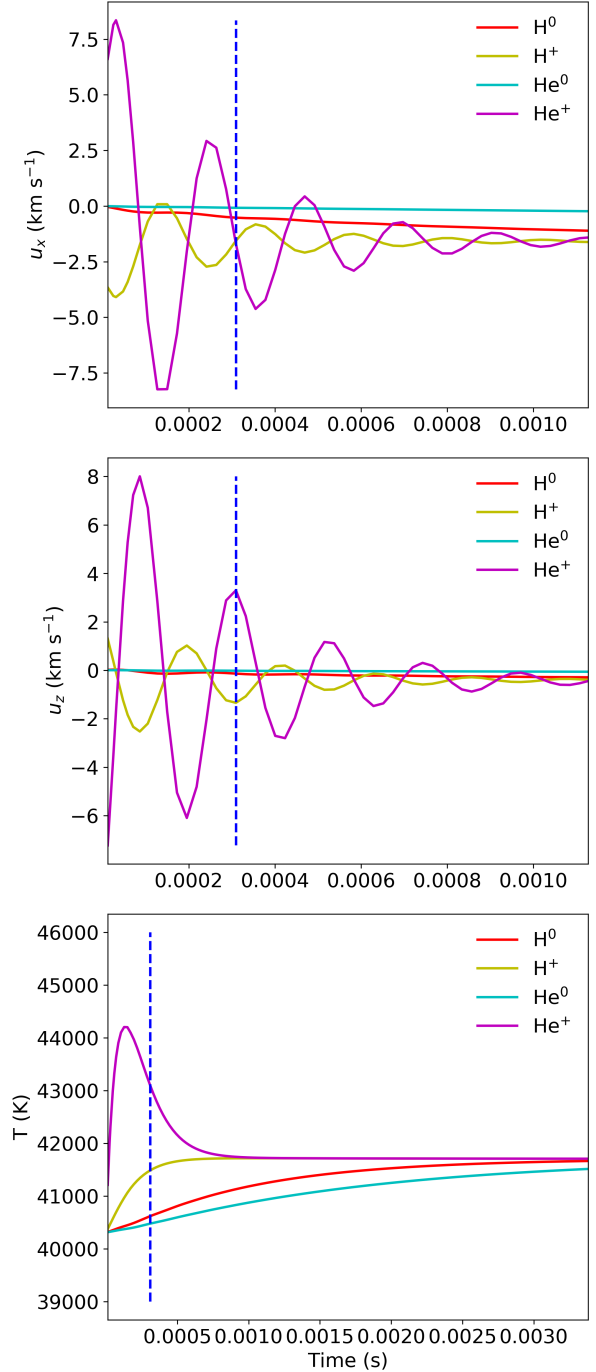


Figure 7. The multi-ion cyclotron wave amplitude is damped due to momentum exchange. Component x (top) and z (middle) of the velocity and temperature (bottom panel) as a function of time for the various energy levels for each species are shown for simulation 1D2S2LCI. Note that the time range of the velocity plots is a subset of the time range shown in the bottom panel (as indicated by the blue line between the bottom and panels and with dashed blue line in the bottom panel).

. In order to drive the Alfvén wave, we impose a temporally varying component with an amplitude of B_x of 0.25 G, *i.e.*, perpendicular to the 1.5D numerical domain. This produced a velocity amplitude of the ions of 800 m s^{-1} (see the second row of Figure 8) propagating along the z -axis. These waves are transverse, but since we are in a 1.5D geometry, they behave as Alfvén waves. We introduced a small amplitude in B_x to mitigate numerical constraints on the time-step (but see below). For 1D2S2LB7, 1D2S2LB8 simulations Alfvén waves are driven at frequencies of 10^3 Hz and we impose an amplitude of B_x of 0.025 G and 2.5 G respectively, producing a velocity amplitude of the ions of 80 m s^{-1} and 8 km s^{-1} , respectively.

Figure 8 shows the velocity drift between the different ionized species (first, fourth and last rows) and the magnetic field (second to last rows) for 1D2S2LB3, 1D2S2LB4, 1D2S2LB5, and 1D2S2LB6 simulations (left to right columns, respectively). Even for driven Alfvén wave frequencies smaller than the multi-ion cyclotron frequency (D2S2LB3, 1D2S2LB4, and 1D2S2LB5) a velocity drift between the two ionized fluids appears in the component perpendicular to the background magnetic field and to the imposed Alfvén wave plane, *i.e.*, y . The velocity drift results from the fact that the inertia of and the forces acting on various ionized species are different.

The velocity drift frequencies match the imposed Alfvén wave frequency in all experiments. Therefore, the frequency of the velocity drift does not depend on multi-ion cyclotron waves as was the case in the previous experiments in previous sections where we imposed an initial velocity drift.

The absolute velocity drift increases with the driven Alfvén wave frequency as long as these frequencies are lower than multi-ion cyclotron frequencies. In addition, the velocity field changes components (*i.e.*, from u_y to u_x) when the driven Alfvén wave frequency is greater than multi-ion cyclotron frequency. In other words, for frequencies greater than multi-ion cyclotron frequencies (1D2S2LB6), time is too short to produce the coupling between the ionized species and the current (and $\vec{J} \times \vec{B}$ in the momentum equation) dominates. Therefore, the velocity drift component corresponds to the $\vec{J} \times \vec{B}$ component. The Lorentz force leads to a velocity drift due to the different inertia, number of ionized particles and charge between the different ionized species (see Equation 17).

As the waves propagate in space, the components of velocity and magnetic field disturbance are transposed to the other component perpendicular to the direction of propagation. This other orthogonal component (y for magnetic field, x for velocity) increases with space in an oscillatory fashion. The length scale (along the propagation direction, z) over which this transposition from x to y (or y to x) occurs depends on the driven

Alfvén frequency: it decreases for increasing frequency. In other words, the higher the frequency, the shorter the distance over which the transfer from x to y occurs.

Figure 9 shows the linear dependence of the component y of the velocity drift with the driver frequency. Simulations 1D2S2LB5, 1D2S2LB7 and 1D2S2LB8 show an increase/decrease of the ion velocity drift with the same factor as the increase/decrease of the driving amplitude. Therefore, for a driven frequency of 10^3 Hz , $\Delta B_x = 2.5 \text{ G}$, and $B_z = 10 \text{ G}$ the velocity drift is 1 km s^{-1} and the amplitude of the ion velocity wave is 8 km s^{-1} . The velocity drift appears even for frequencies lower than the multi-ion cyclotron frequency. We also run experiments where we maintained the $|B|/|\Delta B_x|$ ratio, but reduce/increase by an equal amount both $|B|$ and $|\Delta B_x|$. In these cases, for the same imposed Alfvén frequency, the amplitude of the ion velocity drift is the same. In other words, for the same $|B|/|\Delta B_x|$ ratio, the ion velocity drift is equal, be it in a sunspot or in internetwork.

The velocity drift increases linearly with the imposed Alfvén frequency. Observational evidence for Alfvén waves in the solar chromosphere suggests that there is significant power at periods of 3 to 5 min. For such low frequencies, the wave energy in the velocity drift is likely negligible. However, some observations have found evidence for higher frequency waves with periods as short as 45 s (0.15 Hz) in spicules (*e.g.*, Okamoto & De Pontieu 2011). These observations are limited by the cadence of the observations, so that even higher frequencies cannot be excluded by observations. In fact, transition region spectral lines often show significant broadening beyond the thermal width of order 20 km s^{-1} in exposure times as short as 4 s (De Pontieu et al. 2015). If this non-thermal broadening were to be caused by waves, wave frequencies could be significantly higher than 1 Hz. For the modest Alfvén amplitudes studied here ($\Delta B_x = 2.5 \text{ G}$) in a 10 G field, this would lead to velocity drifts of order 2 m s^{-1} , *i.e.*, quite low. However, these waves may continuously drive the ion velocity drift while they travel through the solar atmosphere and therefore will be damped as well.

A zero-order calculation of the dissipated magnetic energy could be done as follows. Assuming these waves are dissipated while traveling from the mid-chromosphere to the transition region at the top of a spicule, *i.e.*, a distance of roughly 4 Mm, (Figure 4) and considering an Alfvén speed of 400 km s^{-1} (De Pontieu et al. 2017), it takes them roughly 10 s to propagate along the spicule. Alfvén waves such as the ones mentioned above, *i.e.*, 10 G guided field, 2.5 G Alfvén amplitudes (equivalent to $\sim 10 \text{ km s}^{-1}$ wave velocity amplitudes) and a frequency of 1 Hz, will continuously drive a velocity drift of $\sim 2 \text{ m s}^{-1}$. Assuming the collisions damp this velocity drift in $\sim 0.01 \text{ s}$ (top panel of Figure 2), the total Alfvén amplitude damped through the chromosphere is 2 km s^{-1} . For a spicule with $\sim 10^{-12} \text{ g cm}^{-3}$ mass den-

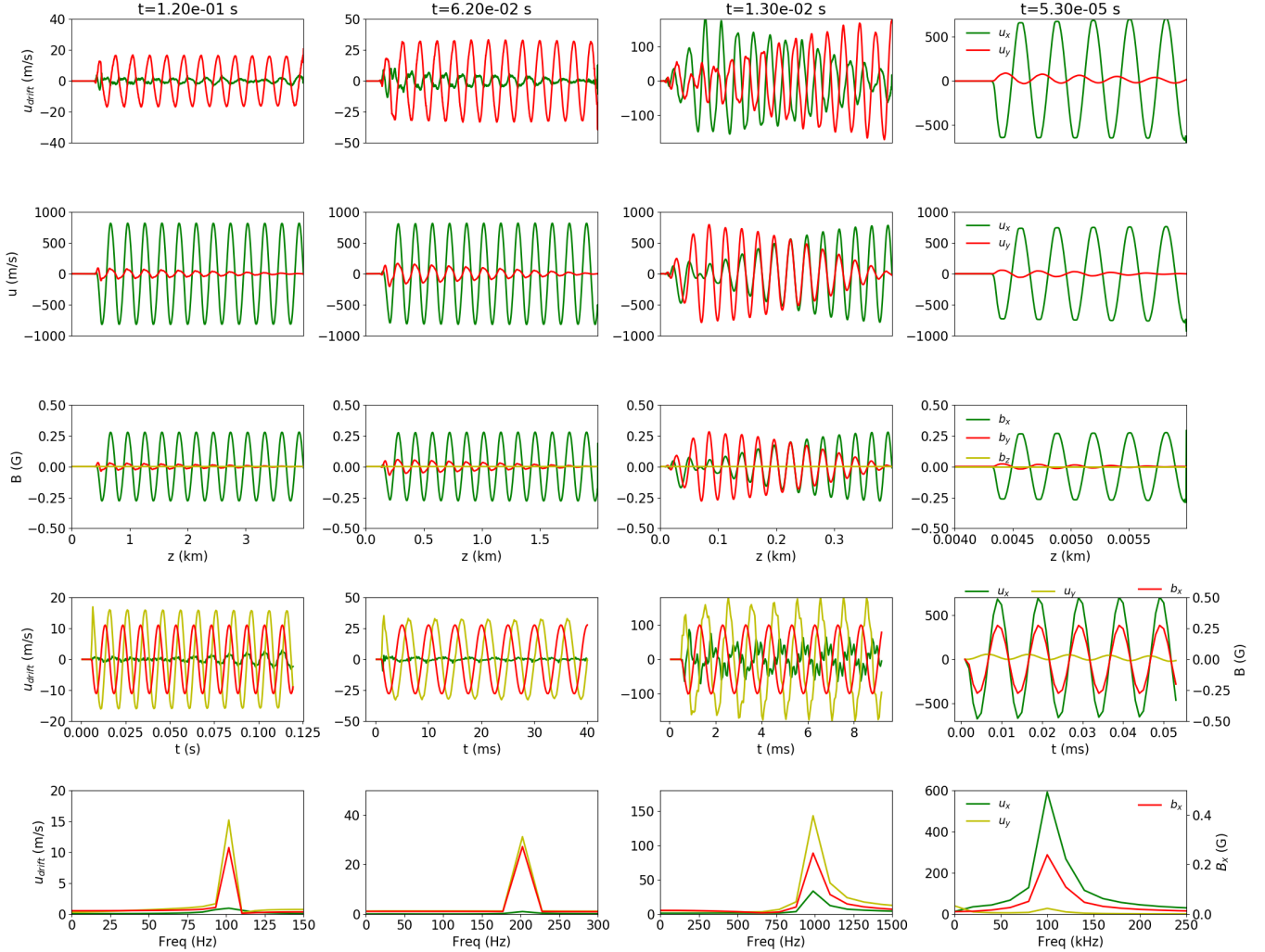


Figure 8. A velocity drift wave is driven by high-frequency Alfvén waves. The velocity drift between the two ionized species as a function of space are shown in the top row, from left to right, for the 1D2S2LB3, 1D2S2LB4, 1D2S2LB5, and 1D2S2LB6 simulations. The total velocity for all ions is shown in the second row. The magnetic field is shown in the third row. We subtracted the initial (10 G) component z of the magnetic field. Fourth and last rows show the velocity (x =green and y =yellow) and x component of the magnetic field (red) as a function of time and frequency, respectively.

sity (middle panel of Figure 1), ~ 300 km wide, and for a length of 4 Mm, the energy dissipated in the spicule is $\sim 3 \cdot 10^{18}$ erg which is $\sim 3 \cdot 10^{17}$ erg s^{-1} , *i.e.*, an energy flux of $\sim 3 \cdot 10^6$ erg $s^{-1} \text{ cm}^{-2}$ (compare with the energy flux needed to maintain the corona De Pontieu et al. 2007). However, this is a back of envelope calculation, and the next step remains to investigate it further in models that contain a stratified atmospheres, *i.e.*, more representative of what is expected to be the situation in the solar atmosphere, and in models where the parameter range for magnetic field strengths and driving wave amplitudes are extended. In addition, momentum exchange between species should also be included.

6. CONCLUSIONS AND DISCUSSION

In a weakly collisional environment, ionized species are coupled through the electric field. So, cyclotron motions occur at multi-ion cyclotron frequencies, which depend on the weighted mass and charge of the ionized species. In addition, the Lorentz force and inertia can act differently on different species. We have developed a new numerical MHD code, called *Ebysus*, that allows us to treat species and their ionized and excited levels separately. This code inherited many features from the *Bifrost* code and shares several numerical characteristics of that code. *Ebysus* allows us to run experiments of interest for this study on multi-ionized species interactions in the solar atmosphere.

In this investigation, we first describe the theory behind multi-ion interactions. This has an analytical solution which is useful for testing the numerical code (*e.g.*,

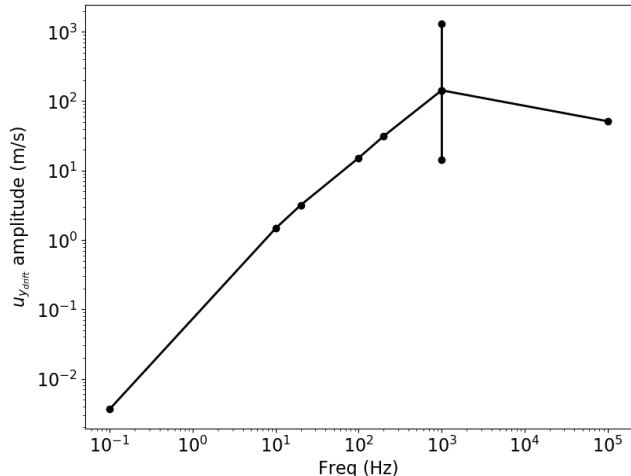


Figure 9. The velocity drift wave amplitude has a linear dependence with the frequency of the driven Alfvén waves for frequencies lower than the multi-ion cyclotron. The top and bottom dots at 10^3 Hz correspond to experiments 1D2S2LB7 and 1D2S2LB8, respectively.

Cramer 2001). An imposed ion-velocity drift can drive multi-ion cyclotron waves. The more species the more superposed multi-ion cyclotron frequencies. These frequencies depend on the number density, cyclotron frequency for each individual ionized species, and particle mass. Then, from so-called realistic radiative MHD models (Martínez-Sykora et al. 2019), we estimated the multi-ion cyclotron frequencies and collision frequencies between different species in the solar atmosphere. We find that these effects may play a role in the upper-chromosphere, TR, and corona. Finally, we calculated highly idealized MFMS numerical experiments in order to understand the coupling between the ionized species through the electric field and its possible role in the solar atmosphere.

The velocity drift between ionized species naturally occurs via Alfvén waves. In principle, as long as there is a significant magnetic tension, e.g. reconnection, species will experience different forces due to the differences in charge and inertia. Preliminary results of magnetic reconnection reveal the presence of ion drift at different stages of the reconnection.

As long as Alfvén waves frequencies are smaller than the multi-ion cyclotron frequencies, the ion-velocity drift increases with increasing Alfvén frequencies. In addition, the ion velocity drift increases with wave amplitude and background magnetic field. Further, the ion velocity drift is invariant for a fix $|B|/|\Delta B_x|$, i.e., in those cases the ion velocity drift is the same in a sunspot or in internetwork. The ion velocity drift might be minor, but there are, at least, three main points to consider in order to estimate if this process can dissipate the wave energy into thermal energy. First, the amplitude of the

waves is not well known, with current observations suggesting amplitudes of, on average, about 20 km s^{-1} . Secondly, the frequency of the observed waves is poorly constrained, with some observations finding evidence for waves of 0.15 Hz on spicules (Okamoto & De Pontieu 2011), and measurements of non-thermal broadening compatible (in principle) with frequencies higher than 1.6 Hz (De Pontieu et al. 2015). Perhaps most importantly, these ion velocity drifts might be continuously generated as long as the Alfvén wave is propagating while at the same time these velocity drifts are being damped by collisions. Therefore, in order to estimate the dissipation of Alfvén waves in the solar atmosphere it is crucial to extend this research by studying models of a stratified atmosphere that includes collisions and a more realistic range of values for various other parameters. High-frequency waves could be driven by magnetic reconnection in the chromosphere (Lazarian & Vishniac 1999). Similarly, the formation of type II spicules is also associated with high-frequency waves (Okamoto & De Pontieu 2011; Martínez-Sykora et al. 2017c).

The ion-velocity drift between ionized species may play a role from the mid-chromosphere to the corona. In addition, these drifts can be dissipated in the chromosphere and transition region and damp high-frequency Alfvén waves and thus contribute in heating spicules and dynamic fibrils (Martínez-Sykora et al. 2019). Chintzoglou et al. (2020) suggested that the simulated spicules may miss extra heating mechanisms. The proposed heating mechanism described here can be also important in the lower corona and it may provide a way to dissipate Alfvén waves generated by spicules and/or reconnection events in the corona, and heat the associated loops (Martínez-Sykora et al. 2017b; De Pontieu et al. 2017; Henriques et al. 2016).

The Alfvén driven models have ion-drifts that can lead to a chemical fractionation. The scope of this study is limited and we have not analyzed this possibility any further. Alfvén driven models have (not shown here) ion velocity drift in the direction of the propagating wave (z-axis). One of the future goals of *Ebysus* is to investigate the First Ionization Potential (FIP) effect and chemical fractionation in the solar atmosphere. Our preliminary results indicate that this code is suited for this research.

This is a very first work on multi-ion cyclotron and ion-drift velocities using highly simplified MFMS numerical simulations. The natural next step is to add complexity to the experiments to address the role of this effect and quantify how important it can be in the solar atmosphere.

7. ACKNOWLEDGMENTS

We gratefully acknowledge support by NASA grants, NNX17AD33G, 80NSSC18K1285, 80NSSC20K1272 and NNG09FA40C (IRIS), NSF grant AST1714955. The simulations have been run on clusters from the Notur project, and the Pleiades cluster through the comput-

ing project s1061, s2053 and s8305 from the High End Computing (HEC) division of NASA. We thankfully acknowledge the support of the Research Council of Nor-

way through grant 230938/F50 and through grants of computing time from the Programme for Supercomputing.

REFERENCES

- Abbo L., Ofman L., Antiochos S. K., et al., 2016, *SSRv*, 201, 55, Slow Solar Wind: Observations and Modeling
- Alvarez Laguna A., Lani A., Deconinck H., Mansour N. N., Poedts S., 2016, *Journal of Computational Physics*, 318, 252, A fully-implicit finite-volume method for multi-fluid reactive and collisional magnetized plasmas on unstructured meshes
- Alvarez Laguna A., Lani A., Mansour N. N., Deconinck H., Poedts S., 2017, *ApJ*, 842, 117, Effect of Radiation on Chromospheric Magnetic Reconnection: Reactive and Collisional Multi-fluid Simulations
- Asplund M., Grevesse N., Sauval A. J., Scott P., 2009, *ARA&A*, 47, 481, The Chemical Composition of the Sun
- Ballester J. L., Alexeev I., Collados M., et al., 2018, *SSRv*, 214, 58, Partially Ionized Plasmas in Astrophysics
- Barakat A. R., Schunk R. W., 1982, *Plasma Physics*, 24, 389, Transport equations for multicomponent anisotropic space plasmas - A review
- Biermann L., 1950, *Zeitschrift Naturforschung Teil A*, 5, 65, Über den Ursprung der Magnetfelder auf Sternen und im interstellaren Raum (miteinem Anhang von A. Schlüter)
- Braginskii S. I., 1965, *Reviews of Plasma Physics*, 1, 205, Transport Processes in a Plasma
- Brandenburg A., Zweibel E. G., 1994, *ApJL*, 427, L91, The formation of sharp structures by ambipolar diffusion
- Brandenburg A., Zweibel E. G., 1995, *ApJ*, 448, 734, Effects of Pressure and Resistivity on the Ambipolar Diffusion Singularity: Too Little, Too Late
- Carlsson M., Stein R. F., 1992, *ApJL*, 397, L59, Non-LTE radiating acoustic shocks and CA II K2V bright points
- Carlsson M., Stein R. F., 2002, *ApJ*, 572, 626, Dynamic Hydrogen Ionization
- Chapman S., Cowling T. G., 1970, The mathematical theory of non-uniform gases. an account of the kinetic theory of viscosity, thermal conduction and diffusion in gases
- Cheung M. C. M., Cameron R. H., 2012, *ApJ*, 750, 6, Magnetohydrodynamics of the Weakly Ionized Solar Photosphere
- Chintzoglou G., Pontieu B. D., Martínez-Sykora J., et al., 2020, IRIS and ALMA Observations Uncovering a Type-II Spicule and the Dynamic Nature of a Chromospheric Plage Region
- Courant R., Friedrichs K., Lewy H., 1928, *Mathematische Annalen*, 100, 32, Über die partiellen Differenzgleichungen der mathematischen Physik
- , 1957, Interscience Publishers N. Y. (ed.), Magnetohydrodynamics. Interscience tracts on physics and astronomy
- Cramer N. F., 2001, *The Physics of Alfvén Waves*. p. 312
- De Pontieu B., De Moortel I., Martínez-Sykora J., McIntosh S. W., 2017, *ApJL*, 845, L18, Observations and Numerical Models of Solar Coronal Heating Associated with Spicules
- De Pontieu B., Martínez-Sykora J., Chintzoglou G., 2017, *ApJL*, 849, L7, What Causes the High Apparent Speeds in Chromospheric and Transition Region Spicules on the Sun?
- De Pontieu B., McIntosh S., Martínez-Sykora J., Peter H., Pereira T. M. D., 2015, *ApJL*, 799, L12, Why is Non-Thermal Line Broadening of Spectral Lines in the Lower Transition Region of the Sun Independent of Spatial Resolution?
- De Pontieu B., McIntosh S. W., Carlsson M., et al., 2007, *Science*, 318, 1574, Chromospheric Alfvénic Waves Strong Enough to Power the Solar Wind
- Demars H. G., Schunk R. W., 1979, *Journal of Physics D Applied Physics*, 12, 1051, Transport equations for multispecies plasmas based on individual bi-Maxwellian distributions
- Demars H. G., Schunk R. W., 1994, *J. Geophys. Res.*, 99, 2215, A multi-ion generalized transport model of the polar wind
- Dzhililov N. S., Kuznetsov V. D., Staude J., 2008, *A&A*, 489, 769, Wave instabilities in an anisotropic magnetized space plasma
- Echim M. M., Lemaire J., Lie-Svendsen Ø., 2011, *Surveys in Geophysics*, 32, 1, A Review on Solar Wind Modeling: Kinetic and Fluid Aspects
- Fontenla J. M., Avrett E. H., Loeser R., 1990, *ApJ*, 355, 700, Energy balance in the solar transition region. I - Hydrostatic thermal models with ambipolar diffusion
- Ganguli S. B., 1996, *Reviews of Geophysics*, 34, 311, The polar wind
- Glassgold A. E., Krstić P. S., Schultz D. R., 2005, *ApJ*, 621, 808, $H^+ + H$ Scattering and Ambipolar Diffusion Heating

- Golding T. P., Carlsson M., Leenaarts J., 2014, *ApJ*, 784, 30, Detailed and Simplified Nonequilibrium Helium Ionization in the Solar Atmosphere
- Golding T. P., Leenaarts J., Carlsson M., 2016, *ApJ*, 817, 125, Non-equilibrium Helium Ionization in an MHD Simulation of the Solar Atmosphere
- Gudiksen B. V., Carlsson M., Hansteen V. H., et al., 2011, *A&A*, 531, A154, The stellar atmosphere simulation code Bifrost. Code description and validation
- Hansteen V. H., Leer E., Holzer T. E., 1997, *ApJ*, 482, 498, The Role of Helium in the Outer Solar Atmosphere
- Henriques V. M. J., Kuridze D., Mathioudakis M., Keenan F. P., 2016, *ApJ*, 820, 124, Quiet-Sun $H\alpha$ Transients and Corresponding Small-scale Transition Region and Coronal Heating
- Hollweg J. V., Isenberg P. A., 2002, *Journal of Geophysical Research (Space Physics)*, 107, 1147, Generation of the fast solar wind: A review with emphasis on the resonant cyclotron interaction
- Hyman J., Vichnevsky R., Stepleman R., 1979, *Adv. in Comp. Meth, PDE's-III*, 313
- Isenberg P. A., Hollweg J. V., 1982, *J. Geophys. Res.*, 87, 5023, Finite amplitude Alfvén waves in a multi-ion plasma - Propagation, acceleration, and heating
- Khomenko E., Collados M., 2012, *ApJ*, 747, 87, Heating of the Magnetized Solar Chromosphere by Partial Ionization Effects
- Khomenko E., Collados M., Díaz A., Vitas N., 2014, *Physics of Plasmas*, 21, 092901, Fluid description of multi-component solar partially ionized plasma
- Koch B. P., Witt M., Engbrodt R., Dittmar T., Kattner G., 2005, *GeoCoA*, 69, 3299, Molecular formulae of marine and terrigenous dissolved organic matter detected by electrospray ionization Fourier transform ion cyclotron resonance mass spectrometry
- Krstic P. S., Schultz D. R., 1999, *Journal of Physics B Atomic Molecular Physics*, 32, 2415, Elastic and vibrationally inelastic slow collisions: $H + H_2$, $H^+ + H_2$
- Krtićka J., Kubát J., 2000, *A&A*, 359, 983, Isothermal two-component stellar wind of hot stars
- Krtićka J., Kubát J., 2001, *A&A*, 369, 222, Multicomponent radiatively driven stellar winds. I. Nonisothermal three-component wind of hot B stars
- Lazarian A., Vishniac E. T., 1999, *ApJ*, 517, 700, Reconnection in a Weakly Stochastic Field
- Lazarian A., Vishniac E. T., Cho J., 2004, *ApJ*, 603, 180, Magnetic Field Structure and Stochastic Reconnection in a Partially Ionized Gas
- Leake J. E., Arber T. D., Khodachenko M. L., 2005, *A&A*, 442, 1091, Collisional dissipation of Alfvén waves in a partially ionised solar chromosphere
- Leake J. E., DeVore C. R., Thayer J. P., et al., 2014, *SSRv*, 184, 107, Ionized Plasma and Neutral Gas Coupling in the Sun's Chromosphere and Earth's Ionosphere/Thermosphere
- Leake J. E., Linton M. G., 2013, *ApJ*, 764, 54, Effect of Ion-Neutral Collisions in Simulations of Emerging Active Regions
- Leake J. E., Lukin V. S., Linton M. G., 2013, *Physics of Plasmas*, 20, 061202, Magnetic reconnection in a weakly ionized plasma
- Leenaarts J., Wedemeyer-Böhm S., Carlsson M., Hansteen V. H., 2007, Non-equilibrium hydrogen ionisation in the solar atmosphere, en Coimbra Solar Physics Meeting ion the Physics of Chromospheric Plasmas, ASP Conference Series, Vol. in this volume, This volume
- Li B., Li X., 2007, *ApJ*, 661, 1222, Propagation of Non-Wentzel-Kramers-Brillouin Alfvén Waves in a Multicomponent Solar Wind with Differential Ion Flow
- Li B., Li X., 2008, *ApJ*, 682, 667, Effects of Non-WKB Alfvén Waves on a Multicomponent Solar Wind with Differential Ion Flow
- Maneva Y. G., Alvarez Laguna A., Lani A., Poedts S., 2017, *ApJ*, 836, 197, Multi-fluid Modeling of Magnetosonic Wave Propagation in the Solar Chromosphere: Effects of Impact Ionization and Radiative Recombination
- Martínez-Gómez D., Soler R., Terradas J., 2016, *ApJ*, 832, 101, Multi-fluid Approach to High-frequency Waves in Plasmas: I. Small-amplitude Regime in Fully Ionized Medium
- Martínez-Gómez D., Soler R., Terradas J., 2017, *ApJ*, 837, 80, Multi-fluid Approach to High-frequency Waves in Plasmas. II. Small-amplitude Regime in Partially Ionized Media
- Martínez-Sykora J., De Pontieu B., Carlsson M., et al., 2017a, *ApJ*, 847, 36, Two-dimensional Radiative Magnetohydrodynamic Simulations of Partial Ionization in the Chromosphere. II. Dynamics and Energetics of the Low Solar Atmosphere
- Martínez-Sykora J., De Pontieu B., De Moortel I., Hansteen L. H. M., Carlsson M., 2017b, *ApJ*, Submitted, Impact of type II spicules in the corona: Simulations and synthetic observables
- Martínez-Sykora J., De Pontieu B., Hansteen V., 2012, *ApJ*, 753, 161, Two-dimensional Radiative Magnetohydrodynamic Simulations of the Importance of Partial Ionization in the Chromosphere

- Martínez-Sykora J., De Pontieu B., Hansteen V., Carlsson M., 2015, *Philosophical Transactions of the Royal Society of London Series A*, 373, 40268, The role of partial ionization effects in the chromosphere
- Martínez-Sykora J., De Pontieu B., Hansteen V. H., et al., 2017c, *Science*, 356, 1269, On the generation of solar spicules and Alfvénic waves
- Martínez-Sykora J., Leenaarts J., De Pontieu B., et al., 2019, arXiv e-prints, arXiv:1912.06682, Ion-neutral interactions and non-equilibrium ionization in the solar chromosphere
- Nóbrega-Siverio D., Martínez-Sykora J., Moreno-Insertis F., Carlsson M., 2020a, arXiv e-prints, arXiv:2004.11927, Ambipolar diffusion in the Bifrost code
- Nóbrega-Siverio D., Moreno-Insertis F., Martínez-Sykora J., Carlsson M., Szydlarski M., 2020b, *A&A*, 633, A66, Nonequilibrium ionization and ambipolar diffusion in solar magnetic flux emergence processes
- Ofman L., Davila J. M., Nakariakov V. M., ViñAs A. F., 2005, *Journal of Geophysical Research (Space Physics)*, 110, A09102, High-frequency Alfvén waves in multi-ion coronal plasma: Observational implications
- Okamoto T. J., De Pontieu B., 2011, *ApJL*, 736, L24, Propagating Waves Along Spicules
- Olsen E. L., Leer E., 1999, *J. Geophys. Res.*, 104, 9963, A study of solar wind acceleration based on gyrotropic transport equations
- Parker E. N., 2007, *Conversations on Electric and Magnetic Fields in the Cosmos*. Princeton University Press
- Rahbarnia K., Ullrich S., Sauer K., Grulke O., Klinger T., 2010, *Physics of Plasmas*, 17, 032102, Alfvén wave dispersion behavior in single- and multicomponent plasmas
- Schultz D. R., Krstic P. S., Lee T. G., Raymond J. C., 2008, *ApJ*, 678, 950, Momentum Transfer and Viscosity from Proton-Hydrogen Collisions Relevant to Shocks and Other Astrophysical Environments
- Schunk R. W., 1977, *Reviews of Geophysics and Space Physics*, 15, 429, Mathematical structure of transport equations for multispecies flows
- Smith R. K., Hughes J. P., 2010, *ApJ*, 718, 583, Ionization Equilibrium Timescales in Collisional Plasmas
- Vernazza J. E., Avrett E. H., Loeser R., 1981, *ApJS*, 45, 635, Structure of the solar chromosphere. III - Models of the EUV brightness components of the quiet-sun
- Vranjes J., Krstic P. S., 2013, *A&A*, 554, A22, Collisions, magnetization, and transport coefficients in the lower solar atmosphere
- Vranjes J., Poedts S., Pandey B. P., de Pontieu B., 2008, *A&A*, 478, 553, Energy flux of Alfvén waves in weakly ionized plasma
- Weber E. J., 1973, *Ap&SS*, 20, 391, Multi-Ion Plasmas in Astrophysics. I: General Requirements for the Existence of Critical Points
- Xie H., Ofman L., ViñAs A., 2004, *Journal of Geophysical Research (Space Physics)*, 109, A08103, Multiple ions resonant heating and acceleration by Alfvén/cyclotron fluctuations in the corona and the solar wind